Dispersive and Nonhydrostatic Pressure Effects at the Front of Surge

Dae-Hong Kim[1] and Patrick J. Lynett[2]

Abstract: Undular bores and shocks generated by dam-break flows or tsunamis are examined considering nonhydrostatic pressure and dispersive effects in one- and two-horizontal-dimensional space. The fully nonlinear Boussinesq-type equations based on a weakly nonhydrostatic pressure assumption are chosen as the governing equations. The equation set is solved by a fourth-order accurate finite-volume method with an approximate Riemann solver. Several typical benchmark problems such as dam-break flows and tsunami wave fission are tested in one- and two-horizontal-dimensional space. The computed results by the Boussinesq-type model are at least as accurate as the results by the hydrostatic shallow water equations. This is particularly evident near the steep front of the wave, where frequency dispersion can play an important role. The magnitude of this nonhydrostatic pressure and dispersive effect near the front is quantified, and the engineering implications of neglecting these physics, as would be done through the use of a hydrostatic model, are discussed. **DOI: 10.1061/(ASCE)HY.1943-7900.0000345.**

CE Database subject headings: Tsunamis; Hydrostatic pressure; Dam failures; Storm surges.

Author keywords: Undular bore; Dam-break flow; Tsunami; Nonhydrostatic pressure; Dispersion; Boussinesq-type equations; Finite-volume method.

Introduction

Every year, human lives, public facilities, and private property are lost to natural hazards related with water flows. Among them, dam-break flows, levee failures, and tsunamis can cause catastrophic damage. Thus, to the hydraulic and coastal engineer, the investigation and prediction of hydraulic bores has been an important issue for a very long time. To find countermeasures for prevention or mitigation, many laboratory experiments and mathematical and numerical studies were performed by numerous research groups (e.g., Ioualalen et al. 2007).

In a typical study for dam-break flows, the initial condition is given following Fig. 1(a), in which two stationary water bodies are separated by a barrier, and the barrier is assumed to be removed instantaneously. To predict the flows numerically, the shallow water wave equations (SWE) are the most common choice. The SWE model assumes that the pressure is dependent only on the total water depth, and the vertical velocity is small enough to be ignored; leading of course to a hydrostatic and nondispersive equation model. With those assumptions, the SWE model can predict a surge and a rarefaction wave, as shown in Fig. 1(b).

However, the secondary phenomena—the undular bore waves generated at the wave front—as shown in Fig. 1(c), are frequently observed in nature. For example, in the Main-Danube navigation canal, secondary waves with a wavelength of approximately 100 m and amplitudes up to ∓ 0.5 m produced by the operation of lock gates have been observed (Treske 1994). Other undular bores have been reported in coastal areas. Undular tidal bores are regularly created in many estuaries, such as in the Qiantang River in China. During large tsunamis, the leading waves can undergo a undular bore process, and this is sometimes termed wave fission (e.g., Matsuyama et al. 2007), although the physical process is the same. Some of the most notable occurrencess are recorded during the 2004 Indian Ocean tsunami (e.g., Grue et al. 2008). The undular motions can lead to significant engineering and design challenges, as the process can lead to a larger leading wave crest. These water surface undulations cannot be predicted by a SWE model based on the hydrostatic pressure assumption, because they are dispersive in nature.

An option for dispersive wave simulation is the Boussinesq-type model. This model is, in essence, the SWE model with a second-order correction to account for weakly nonhydrostatic physics. Like the SWE, Boussinesq-type models are depth-integrated and thus can be solved efficiently across large spatial domains. Assuming that both nonlinearity and frequency dispersion are weak and are in the same order of magnitude, Peregrine (1967) derived the "standard" Boussinesq equations for variable depth in the depth-averaged velocity and the free-surface displacement. Numerical results based on the standard Boussinesq equations or the equivalent formulations have been shown to give predictions that compared quite well for a range of physical configurations (e.g., Goring 1978), including undular bore evolution (Soares-Frazao and Zech 2002b). Because it is required that both frequency dispersion and nonlinear effects are weak, the standard Boussinesq equations are not applicable to very shallow water depth, in which the nonlinearity becomes more important than the frequency dispersion.

As waves travel upslope, wave height increases because of shoaling until eventually breaking. The wave height to water-depth ratios associated with this physical process violates the weakly nonlinear assumption. This restriction can be readily removed by eliminating the weak nonlinearity assumption (e.g., Liu 1994; Wei et al. 1995), yielding the fully nonlinear Boussinesq-type model.

[1]Assistant Professor, Dept. of Civil Engineering, Univ. of Seoul, Seoul, Republic of Korea (corresponding author). E-mail: dhkimhyd@uos.ac.kr

[2]Associate Professor, Zachry Dept. of Civil Engineering, Texas A&M Univ., College Station, TX.

Note. This manuscript was submitted on March 4, 2010; approved on October 10, 2010; published online on December 21, 2010. Discussion period open until December 1, 2011; separate discussions must be submitted for individual papers. This paper is part of the ***Journal of Hydraulic Engineering***, Vol. 137, No. 7, July 1, 2011. ©ASCE, ISSN 0733-9429/2011/7-754–765/$25.00.

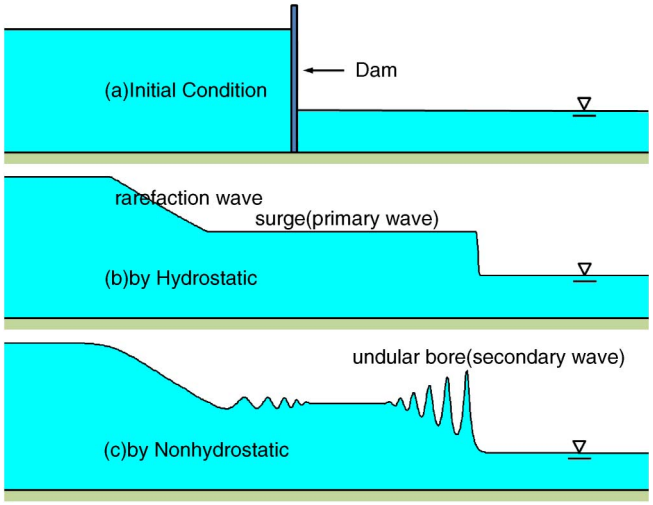

Fig. 1. Schematics of water surface profile patterns by a typical dam-break problem: (a) initial condition; (b) profile by hydrostatic theory; (c) profile by nonhydrostatic theory

Although there is no precise nonlinear accuracy limitation of the weakly nonlinear Boussinesq (WNB) model, as it depends on a range of physical properties, in general it is assumed that the fully nonlinear Boussinesq (FNB) model should be used if the wave height to water-depth ratio exceeds 0.3 (e.g., Wei et al. 1995). Application of the FNB equations is widespread, including rip and longshore currents, wave run-up (Lynett et al. 2002), wave-current interaction (Ryu et al. 2003), among many others.

Conceptually, Soares-Frazao and Zech (2002b) described the effect of nonhydrostatic pressure on undular bores and modeled the fluid motions with both a laboratory experiment and a numerical model based on the WNB equations. Using long wave scaling, a simple mathematical expression of the pressure in a Boussinesq-type model is given by (e.g., Wei et al. 1995)

$$\frac{p}{\rho g} = \zeta - z + \frac{1}{2}(z^2 - \zeta^2)\frac{\partial S}{\partial t} + (z - \zeta)\frac{\partial T}{\partial t} + \frac{1}{2}(z^2 - \zeta^2)\boldsymbol{U}\cdot\nabla S + (z - \zeta)\boldsymbol{U}\cdot\nabla T + \frac{1}{2}(\zeta^2 - z^2)S^2 + (\zeta - z)TS \quad (1)$$

where g = gravitational acceleration; ρ = water density; z = vertical direction; and the ζ is the water surface elevation; $\boldsymbol{U} = (U, V)$ = horizontal velocities evaluated at an arbitrary level $z = z_\alpha(x, y)$ in the x and y direction, respectively; t = time; $\nabla = (\partial/\partial x, \partial/\partial y)$; $S = (\partial U/\partial x + \partial V/\partial y)$; $T = (\partial hU/\partial x + \partial hV/\partial y)$, where h = local water depth. As can be seen from Eq. (1), the pressure depends not only on the water depth but also on the spatial and time variations of the fluid velocity and the total water depth. As the leading portion of dam-break flows, tidal bores, and some tsunamis are strongly transient and nonuniform, the third and later terms on the right-hand side of Eq. (1) may be significant.

Recently, Mohapatra and Chaudhry (2004) presented the effect of nonhydrostatic pressure effects on two dam-break flow configurations by using a WNB model. They solved the equations with a fourth-order explicit finite-difference method (FDM). In their results, the computed water surface profiles had undulations when the depth ratio ε(= downstream water depth/upstream water depth) was greater than 0.4. A main conclusion of their effort was that the SWE provided sufficiently accurate results for the maximum flow depth and the arrival time of the flood wave; the differences between the SWE and Boussinesq model were negligibly minor. Carmo et al. (1993) conducted dam-break flow experiments with the condition of $\varepsilon > 0.5$ and observed undular bores downstream of the dam. They compared the experimental data and computed results based on a the weakly dispersive Serre equations, and achieved good results. Mignot and Cienfuegos (2009) applied a one-horizontal-dimension (1HD) Boussinesq model that included wave-breaking energy dissipation. However, their applications were not specifically for undular bores, and they did not examine this process.

Undular bores generated by a sudden release of a constant discharge were investigated by Soares-Frazao and Zech (2002b) with an experiment and a numerical method. They solved the 1HD WNB equations with a hybrid finite-volume method (FVM) and FDM (FDM/FDM) numerical scheme. Soares-Frazao and Guinot (2008) proposed a modified hybrid scheme to solve the WNB equations in 1HD space on a horizontal bed. More accurate computed results than the results by the previous hybrid model were obtained. Soares-Frazao and Zech (1998, 2002a) also presented two-horizontal-dimension (2HD) experimental and numerical results of a dam-break flow in a channel with a 90° bend. Here, however, the numerical model was based on the SWE. They showed that the 1HD results were of limited usefulness, whereas the 2HD model provided additional physical information and rather satisfactory prediction.

Large tsunamis can cause immense coastal damage. When approaching a coastline, the steepness of the leading wave becomes greater because of shoaling. If steepening is significant, vertical accelerations can become large and nonhydrostatic effects correspondingly relevant. Consequently, undular bores (i.e., soliton fission) can be generated in nearshore areas. For example, fission was observed during the 1983 Nihonkai-Chubu earthquake tsunami in Japan (Shuto 1985). These waves can lead to harbor oscillation problems or can affect run-up height, which is critical to evacuation. To predict these secondary wave motions numerically, the nonhydrostatic pressure effects must be accounted for in the governing equations.

In this paper, several benchmark problems of undular bores are simulated by using a fully nonlinear Boussinesq-type model in 1HD and 2HD space. The governing equations and the numerical methods are briefly introduced. In the following section, numerical results are presented and compared with measured data to show the ability of the present Boussinesq-type equations model for the application to the undular bores. Discussion of the results follows, and the engineering implications are outlined.

Boussinesq-Type Equations

Fully Nonlinear Boussinesq-Type Equations

The fully nonlinear, weakly dispersive, weakly rotational Boussinesq-type equations of Kim et al. (2009) in conservative form are given by

$$\frac{\partial H}{\partial t} + \frac{\partial HU}{\partial x} + \frac{\partial HV}{\partial y} + \mathcal{C} = 0 \quad (2)$$

$$\frac{\partial HU}{\partial t} + \frac{\partial HU^2}{\partial x} + \frac{\partial HUV}{\partial y} + gH\frac{\partial \zeta}{\partial x} + H\mathcal{M} + U\mathcal{C} = H\nabla\cdot(\nu_t^h\nabla\boldsymbol{U}) - H\nu_t^v\nabla S - \frac{\tau_x^b}{\rho} \quad (3)$$

$$\frac{\partial HV}{\partial t} + \frac{\partial HUV}{\partial x} + \frac{\partial HV^2}{\partial y} + gH\frac{\partial \zeta}{\partial y} + H\mathcal{M} + V\mathcal{C} = H\nabla\cdot(\nu_t^h\nabla\boldsymbol{U}) - H\nu_t^v\nabla S - \frac{\tau_y^b}{\rho} \quad (4)$$

J. Hydraul. Eng. 2011.137:754-765.

where $H = \zeta + h$ is the total water depth. The $\mathcal{C}$ in the depth-integrated continuity equation is given by

$$\mathcal{C} = -\nabla \cdot \left(H \left\{ \left[\frac{(\zeta^2 - \zeta h + h^2)}{6} - \frac{z_\alpha^2}{2} \right] \nabla S + \left[\frac{(\zeta - h)}{2} - z_\alpha \right] \nabla T \right\} \right) + \nabla \cdot \left\{ \psi H \left[\frac{z_\alpha^2}{2} - z_\alpha \zeta + \frac{(2\zeta^2 - 2\zeta h - h^2)}{6} \right] \right\} \quad (5)$$

in which $\psi = \tau^b / \{\nu_t^v (\zeta + h)\}$. In the momentum equations, the $\mathcal{M}$ is given by

$$\mathcal{M} = \boldsymbol{D} + \boldsymbol{D}^v + \bar{\boldsymbol{\xi}} + \bar{\boldsymbol{\xi}}^{\bar{\nu}} \quad (6)$$

in which

$$\boldsymbol{D} = \frac{1}{2} \nabla (z_\alpha^2 \boldsymbol{U} \cdot \nabla S) + \nabla (z_\alpha \boldsymbol{U} \cdot \nabla T) + (T \nabla T) - \frac{1}{2} \nabla \left(\zeta^2 \frac{\partial S}{\partial t} \right) - \nabla \left(\zeta \frac{\partial T}{\partial t} \right) + \left(\frac{1}{2} z_\alpha^2 \frac{\partial \nabla S}{\partial t} + z_\alpha \frac{\partial \nabla T}{\partial t} \right) - \frac{1}{2} \nabla (\zeta^2 \boldsymbol{U} \cdot \nabla S) - \nabla (\zeta \boldsymbol{U} \cdot \nabla T) + \nabla \left(\frac{1}{2} \zeta^2 S^2 \right) + \nabla (\zeta T S) \quad (7)$$

$$\boldsymbol{D}^v = \frac{(\zeta - h)}{2} \frac{\partial \psi |\zeta}{\partial t} - \frac{(\zeta^2 - \zeta h + h^2)}{6} \frac{\partial \psi}{\partial t} + \frac{\partial}{\partial t} \left[\psi \left(\frac{z_\alpha^2}{2} - \zeta z_\alpha \right) \right] + \frac{(\zeta - h)}{2} \nabla [\boldsymbol{U} \cdot (\psi \zeta)] - \frac{(\zeta^2 - \zeta h + h^2)}{6} \nabla (\boldsymbol{U} \cdot \psi) + \nabla \left\{ \boldsymbol{U} \cdot \left[\psi \left(\frac{z_\alpha^2}{2} - \zeta z_\alpha \right) \right] \right\} - \psi \left[\frac{(\zeta^2 + \zeta h - 2h^2) S}{6} + \frac{(\zeta + h) T}{2} \right] \quad (8)$$

$$\bar{\xi}^x = -V \left[\frac{\partial z_\alpha}{\partial x} \left(z_\alpha \frac{\partial S}{\partial y} + \frac{\partial T}{\partial y} \right) - \frac{\partial z_\alpha}{\partial y} \left(z_\alpha \frac{\partial S}{\partial x} + \frac{\partial T}{\partial x} \right) \right] - \left(\frac{\partial V}{\partial x} - \frac{\partial U}{\partial y} \right) \left\{ \left[\frac{z_\alpha^2}{2} - \frac{(\zeta^2 - \zeta h + h^2)}{6} \right] \frac{\partial S}{\partial y} + \left[z_\alpha - \frac{(\zeta - h)}{2} \right] \frac{\partial T}{\partial y} \right\} \quad (9)$$

$$\bar{\xi}^y = U \left[\frac{\partial z_\alpha}{\partial x} \left(z_\alpha \frac{\partial S}{\partial y} + \frac{\partial T}{\partial y} \right) - \frac{\partial z_\alpha}{\partial y} \left(z_\alpha \frac{\partial S}{\partial x} + \frac{\partial T}{\partial x} \right) \right] + \left(\frac{\partial V}{\partial x} - \frac{\partial U}{\partial y} \right) \left\{ \left[\frac{z_\alpha^2}{2} - \frac{(\zeta^2 - \zeta h + h^2)}{6} \right] \frac{\partial S}{\partial x} + \left[z_\alpha - \frac{(\zeta - h)}{2} \right] \frac{\partial T}{\partial x} \right\} \quad (10)$$

$$\bar{\xi}^{\bar{\nu}^x} = -V \left\{ \frac{\partial}{\partial x} \left[\psi^y \left(\frac{1}{2} z_\alpha^2 - z_\alpha \zeta \right) \right] - \frac{(\zeta^2 - \zeta h + h^2)}{6} \frac{\partial \psi^y}{\partial x} + \frac{(\zeta - h)}{2} \frac{\partial \psi^y \zeta}{\partial x} - \frac{\partial}{\partial y} \left[\psi^x \left(\frac{1}{2} z_\alpha^2 - z_\alpha \zeta \right) \right] + \frac{(\zeta^2 - \zeta h + h^2)}{6} \frac{\partial \psi^x}{\partial y} - \frac{(\zeta - h)}{2} \frac{\partial \psi^x \zeta}{\partial y} \right\} - \left(\frac{\partial V}{\partial x} - \frac{\partial U}{\partial y} \right) \psi^y \left[\frac{z_\alpha^2}{2} - z_\alpha \zeta + \frac{(2\zeta^2 - 2\zeta h - h^2)}{6} \right] \quad (11)$$

$$\bar{\xi}^{\bar{\nu}^y} = U \left\{ \frac{\partial}{\partial x} \left[\psi^y \left(\frac{1}{2} z_\alpha^2 - z_\alpha \zeta \right) \right] - \frac{(\zeta^2 - \zeta h + h^2)}{6} \frac{\partial \psi^y}{\partial x} + \frac{(\zeta - h)}{2} \frac{\partial \psi^y \zeta}{\partial x} - \frac{\partial}{\partial y} \left[\psi^x \left(\frac{1}{2} z_\alpha^2 - z_\alpha \zeta \right) \right] + \frac{(\zeta^2 - \zeta h + h^2)}{6} \frac{\partial \psi^x}{\partial y} - \frac{(\zeta - h)}{2} \frac{\partial \psi^x \zeta}{\partial y} \right\} + \left(\frac{\partial V}{\partial x} - \frac{\partial U}{\partial y} \right) \psi^x \left[\frac{z_\alpha^2}{2} - z_\alpha \zeta + \frac{(2\zeta^2 - 2\zeta h - h^2)}{6} \right] \quad (12)$$

where $(\psi^x, \psi^y) = \boldsymbol{\psi}$; $\bar{\boldsymbol{\xi}} = (\bar{\xi}^x, \bar{\xi}^y)$; and $\bar{\boldsymbol{\xi}}^{\bar{\nu}} = (\bar{\xi}^{\bar{\nu}^x}, \bar{\xi}^{\bar{\nu}^y})$. The physical meanings of the high-order terms are explained in Kim et al. (2009)

To approximate the bottom stress, a quadratic friction equation is used

$$\tau_x^b = c_f \rho \tilde{u} \sqrt{\tilde{u}^2 + \tilde{v}^2}, \qquad \tau_y^b = c_f \rho \tilde{v} \sqrt{\tilde{u}^2 + \tilde{v}^2} \quad (13)$$

where the τ_x^b and τ_y^b = bottom shear stresses in the x and y directions, respectively; $\tilde{u}$ and $\tilde{v}$ = depth-averaged velocities. The roughness coefficient is given by $c_f = f/4$ (Chen and Jirka, 1995), and the f is estimated by using the Moody diagram, of which is calculated here by the explicit formula given by Haaland (1983). The Manning friction formula can be applied with $c_f = gn^2/H^{1/3}$, where n is the Manning coefficient. The horizontal subgrid scale dissipation is modeled by using the Smagorinsky model (1963)

$$\nu_t^h = C_s^2 \Delta x \Delta y \left[2 \left(\frac{\partial U}{\partial x} \right)^2 + 2 \left(\frac{\partial V}{\partial y} \right)^2 + 2S^2 + \left(\frac{\partial V}{\partial x} + \frac{\partial U}{\partial y} \right)^2 \right]^{1/2} \quad (14)$$

where, for the Smagorinsky constant, $C_s = 0.2$ is used in this paper. The vertical eddy viscosity is given by

$$\nu_t^v = C_h H u_\tau \quad (15)$$

where $C_h = \kappa/6$ is used, following Elder (1959) with the von Karman constant $\kappa = 0.4$; and u_τ = friction velocity ($u_\tau = \sqrt{\tau^b/\rho}$).

Numerical Scheme

The same numerical method used in Kim et al. (2009) is employed here, with a single but important exception described subsequently. The numerical method uses a fourth-order monotone upstream-centered schemes for conservation laws-total variation diminishing (MUSCL-TVD) scheme to solve the leading-order (shallow water) terms. For the high-order terms, a cell averaged finite-volume method is implemented. For the time integration, the third-order Adams-Bashforth predictor and the fourth-order Adams-Moulton corrector scheme are used.

The predictor step is

$$\zeta^{n+1} = \zeta^n + \frac{\Delta t}{12} (23E^n - 16E^{n-1} + 5E^{n-2}) \quad (16)$$

$$P^{n+1} = P^n + \frac{\Delta t}{12} (23F^n - 16F^{n-1} + 5F^{n-2}) + 2F_1^n - 3F_1^{n-1} + F_1^{n-2} + F_v^p \quad (17)$$

$$Q^{n+1} = Q^n + \frac{\Delta t}{12} (23G^n - 16G^{n-1} + 5G^{n-2}) + 2G_1^n - 3G_1^{n-1} + G_1^{n-2} + G_v^p \quad (18)$$

J. Hydraul. Eng. 2011.137:754-765.

The corrector step is

$$\zeta^{n+1} = \zeta^n + \frac{\Delta t}{24}(9E^{n+1} + 19E^n - 5E^{n-1} + E^{n-2}) \tag{19}$$

$$P^{n+1} = P^n + \frac{\Delta t}{24}(9F^{n+1} + 19F^n - 5F^{n-1} + F^{n-2}) + F_1^{n+1} - F_1^n + F_v^c \tag{20}$$

$$Q^{n+1} = Q^n + \frac{\Delta t}{24}(9G^{n+1} + 19G^n - 5G^{n-1} + G^{n-2}) + G_1^{n+1} - G_1^n + G_v^c \tag{21}$$

where the more detail description of each term can be found in Kim et al. (2009).

The exception noted in the previous paragraph is the Riemann solver component in MUSCL-TVD scheme, which plays a large role in shock capturing simulations. For the calculation of leading-order terms, except for the bottom slope terms gHh_x and gHh_y, a fourth-order compact MUSCL-TVD scheme (Yamamoto and Daiguji, 1993) is used to construct the interface values as follows:

$$\phi_{i+1/2}^L = \phi_i + \frac{1}{6}\{\Delta^*\bar{\phi}_{i-1/2} + 2\Delta^*\tilde{\phi}_{i+1/2}\} \tag{22}$$

$$\phi_{i+1/2}^R = \phi_{i+1} - \frac{1}{6}\{2\Delta^*\bar{\phi}_{i+1/2} + \Delta^*\tilde{\phi}_{i+3/2}\} \tag{23}$$

where

$$\Delta^*\bar{\phi}_{i-1/2} = \text{minmod}(\Delta^*\phi_{i-1/2}, b\Delta^*\phi_{i+1/2}) \tag{24}$$

$$\Delta^*\tilde{\phi}_{i+1/2} = \text{minmod}(\Delta^*\phi_{i+1/2}, b\Delta^*\phi_{i-1/2}) \tag{25}$$

$$\Delta^*\bar{\phi}_{i+1/2} = \text{minmod}(\Delta^*\phi_{i+1/2}, b\Delta^*\phi_{i+3/2}) \tag{26}$$

$$\Delta^*\tilde{\phi}_{i+3/2} = \text{minmod}(\Delta^*\phi_{i+3/2}, b\Delta^*\phi_{i+1/2}) \tag{27}$$

$$\Delta^*\phi_{i+1/2} = \Delta\phi_{i+1/2} - \frac{1}{6}\Delta^3\bar{\phi}_{i+1/2} \tag{28}$$

$$\Delta^3\bar{\phi}_{i+1/2} = \Delta\bar{\phi}_{i-1/2} - 2\Delta\bar{\phi}_{i+1/2} + \Delta\bar{\phi}_{i+3/2} \tag{29}$$

$$\Delta\bar{\phi}_{i-1/2} = \text{minmod}(\Delta\phi_{i-1/2}, b_1\Delta\phi_{i+1/2}, b_1\Delta\phi_{i+3/2}) \tag{30}$$

$$\Delta\bar{\phi}_{i+1/2} = \text{minmod}(\Delta\phi_{i+1/2}, b_1\Delta\phi_{i+3/2}, b_1\Delta\phi_{i-1/2}) \tag{31}$$

$$\Delta\bar{\phi}_{i+3/2} = \text{minmod}(\Delta\phi_{i+3/2}, b_1\Delta\phi_{i-1/2}, b_1\Delta\phi_{i+1/2}) \tag{32}$$

$$\text{minmod}(i,j) = \text{sign}(i)\max\{0, \min[|i|, \text{sign}(i)]\} \tag{33}$$

$$\text{minmod}(i,j,k) = \text{sign}(i)\max\{0, \min[|i|, \text{sign}(i)j, \text{sign}(i)k]\} \tag{34}$$

in which the coefficient $b_1 = 2$; and $1 \le b \le 4$. Additional details of this numerical scheme are described in Yamamoto and Daiguji (1993). By using the constructed interface values, the numerical fluxes are computed by the HLL approximate Riemann solver. The HLL numerical flux is given by (Toro 2002)

$$\boldsymbol{F}_{i+1/2}^{\text{HLL}} = \begin{cases} \boldsymbol{F}_L, & 0 \le S_L \\ \boldsymbol{F}_*, & S_L \le 0 \le S_R \\ \boldsymbol{F}_R, & 0 \ge S_R \end{cases} \tag{35}$$

where

$$\boldsymbol{F}_* = \frac{S_R\boldsymbol{F}_L - S_L\boldsymbol{F}_R + S_RS_L(\boldsymbol{U}_R - \boldsymbol{U}_L)}{S_R - S_L} \tag{36}$$

The wave speeds S_L and S_R are given by

$$S_L = U_L - a_Lq_L, \qquad S_R = U_R + a_Rq_R \tag{37}$$

where the subscripts L and R = left and right computational cells of the interface; and a_L and a_R = long-wave celerities at these interfaces. The q_L is given by

$$q_L = \begin{cases} \sqrt{\frac{1}{2}\frac{(H_*+H_L)H_*}{H_L^2}}, & H_* > H_L \\ 1, & H_* \le H_L \end{cases} \tag{38}$$

where H_* is given by

$$H_* = \frac{1}{g}\left[\frac{1}{2}(a_L + a_R) + \frac{1}{4}(U_L - U_R)\right]^2 \tag{39}$$

The q_R can be obtained in the same manner.

This numerical scheme comprised of Riemann solvers with a MUSCL scheme is highly accurate and stable for shock capturing. However, if applied on a steep sloped or discontinuous bottom, nonphysical numerical oscillations are created even when the limiter is used. To eliminate this numerical oscillation, RSGM, a modified version of the surface gradient method (Kim et al. 2008) that is applicable on steep slopes or discontinuous bathymetry is used in this paper. To describe the wet and dry processes, a moving boundary scheme that can be applied to mild sloped and surface-piercing discontinuous topography is used. The details of the moving boundary scheme is well described in Lynett et al. (2010).

Numerical Simulations and Discussion

In this section, the ability of the numerical model to predict the dynamics at the front of a dam-break flow and tsunami is tested. The validations chosen cover a wide range of 1HD to 2HD problems, from simple bathymetry to complex, and from relatively minor front transformation to extreme, in which both nonlinearity and dispersion are very important. These results will provide a basis on which to compare the presented model with previous studies, and yield the guidance needed to discuss the engineering significance of the phenomena.

Undular Bore Generation by a Sudden Discharge

First, the ability of the developed numerical scheme to predict the formation of an undular bore generated by a sudden release of water in 1HD is investigated. For verification, a laboratory experiment conducted by Soares-Frazao and Zech (2002b) was chosen. In the experiment, a sluice gate was installed between an upstream reservoir and the downstream channel, as shown in Fig. 2. In the downstream channel, six water surface elevation gauges ($C0 \quad \cdots \quad C5$) were installed. The initial downstream water depth

J. Hydraul. Eng. 2011.137:754-765.

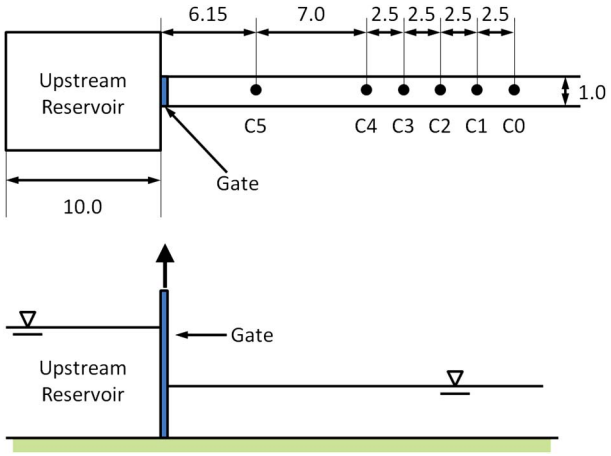

Fig. 2. Experimental setup for undular bore propagation (Soares-Frazao and Guinot 2008, reprinted with permission from Wiley) (all units in meters)

was $h = 0.251$ m. The sluice gate was opened partially from the bottom, thus a sudden discharge was pushed into the downstream channel instantaneously and constantly. For the numerical simulation, this sudden release from the gate was modeled as a unit discharge 0.059 m^2/s at the upstream boundary condition as done by Soares-Frazao and Guinot (2008). The grid size $\Delta x = 0.05$ m, the $C_r = 0.5$, and the roughness height $k_s = 0.0003$ m were used for the numerical simulation.

The time series of the water surface elevations at each gauge are plotted in Fig. 3, showing the experimental results, the numerical WNB results of Soares-Frazao and Guinot (2008), and the FNB results of the model presented here. As can be seen from the images, the physical characteristics of the undular bore are

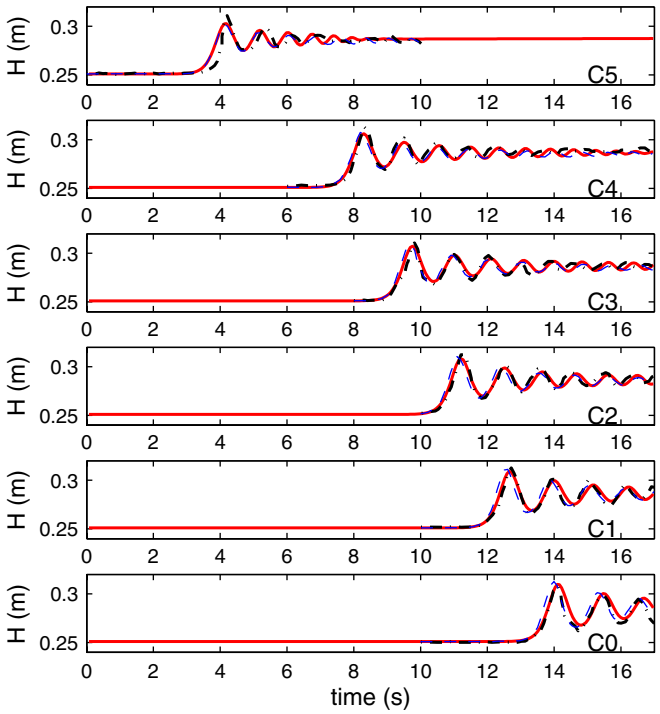

Fig. 3. Time series of water surface at each gauge; thick solid line: present study; thick dash-dotted line: experiment; thin dashed line: by Soares-Frazao and Guinot (2008)

captured very reasonably by both numerical models. In addition, the amplitudes and the periods of the waves agree very well with the experimental data quantitatively. The small difference between the two numerical models is not likely because of the fully nonlinear accuracy of the presented model, which should provide only minor benefits for this wave with height-to-depth ratio of approximately 0.2. It is more likely because of the linear dispersion accuracy of the extended-Boussinesq derivation (Nwogu 1993) that is used in Kim et al. (2009) model.

To test the importance of dispersion effects, the SWE model was applied to solve the same flow. However, as expected, the SWE failed to generate the secondary waves. As can be seen in Fig. 4, the SWE model can generate only the step wave (in the absence of numerical dispersion). The SWE model used in this paper is solved by the same numerical method as used with the Boussinesq-type equation, that is, a fourth-order MUSCL scheme with the Harten, Lax, Van Leer (HLL) approximate Riemann solver. Thus it is able to capture the near-vertical face of the shock, without dispersion errors. Lastly, it is remarked that the height of the leading undular bore wave is 1.7 times that of the upstream water level (also the height of the SWE bore), as measured from the downstream water level.

Dam-Break Flow Simulations

In this test, a gate is fully opened instantaneously so that a rarefaction wave is generated and propagates toward the upstream reservoir. This is different from the previous test case, in which a constant discharge is released from a partially opened gate into a finite downstream depth. For the verification, an experimental case exhibiting undular bores (Carmo et al. 1993) was chosen. The experiment was conducted in a 7.50 m long and flat channel. One water-surface level gauge (G1) was installed in the upstream reservoir at $x = 2.65$ m from the upstream end. The other three gauges (G2–G4) were located at $x = 5.25$ m, 6.25 m, and 7.25 m, respectively, in the downstream channel. The initial upstream reservoir water depth was 0.099 m and the downstream channel water depth was 0.051 m. For the numerical simulations, $\Delta x = 0.01$ m, $C_r = 0.5$, and $k_s = 0.0001$ m were used.

The time series of the water surface elevation are shown in Fig. 5. For the measured data, the values of ζ are not given because they were not reported in Carmo et al. (1993). However, it seems that the FNB model predicts the oscillatory patterns and the periods of the secondary waves very well. As expected, the SWE model provides physics that are incorrect near the bore front because of the hydrostatic pressure assumption.

The small difference of the arrival timing between the experiment and simulation mainly results from the gate opening time (t_{op}). To be regarded as an instantaneous opening, the t_{op} should satisfy (Vischer and Hager 1998)

$$t_{op} \leq 1.25\sqrt{\frac{H_u}{g}} \approx 0.13 \tag{40}$$

where the H_u = initial upstream water depth, and should be in the range (Lauber and Hager 1998)

$$t_{op} \leq \sqrt{\frac{2H_u}{g}} \approx 0.14 \tag{41}$$

In the numerical simulations, t_{op} was assumed to be 0.0 s, but it took approximately $t_{op} = 0.5$ s in the laboratory experiments. Prescribing a "slowly" moving vertical wall is difficult in a

J. Hydraul. Eng. 2011.137:754-765.

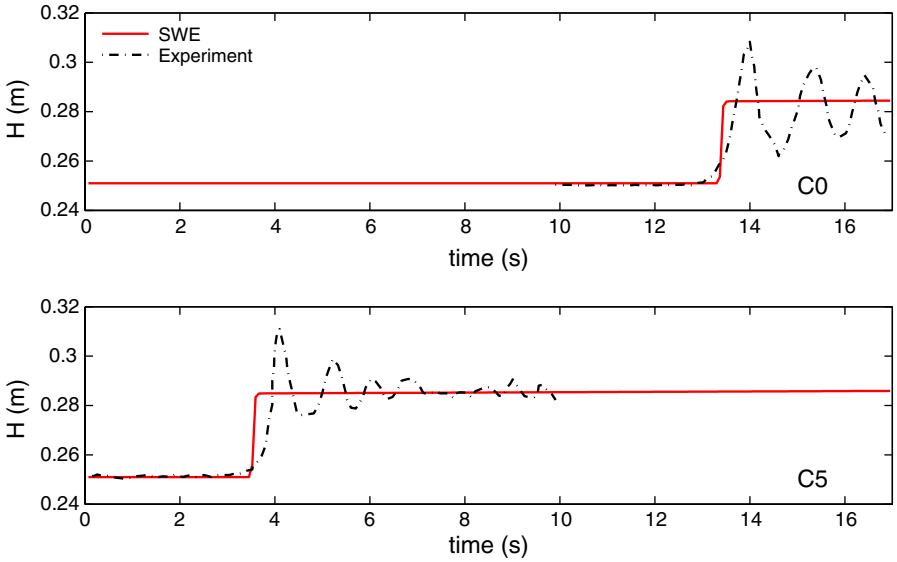

Fig. 4. Time series of water surface at gauges; SWE: by shallow water equations model; experiment: measured data

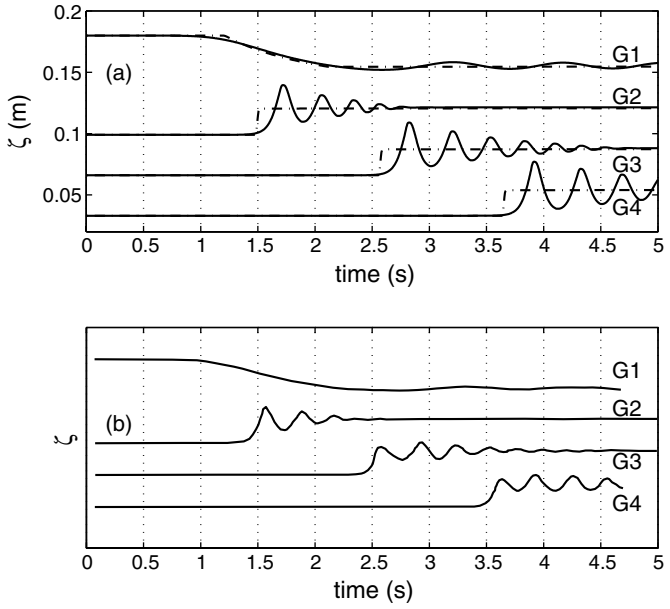

Fig. 5. Time series of water surface elevation: (a) computed results (solid line: by FNB model; dotted line: by SWE model); (b) measured data (Carmo et al. 1993) (G1, G2, G3, and G4 are the gauge numbers)

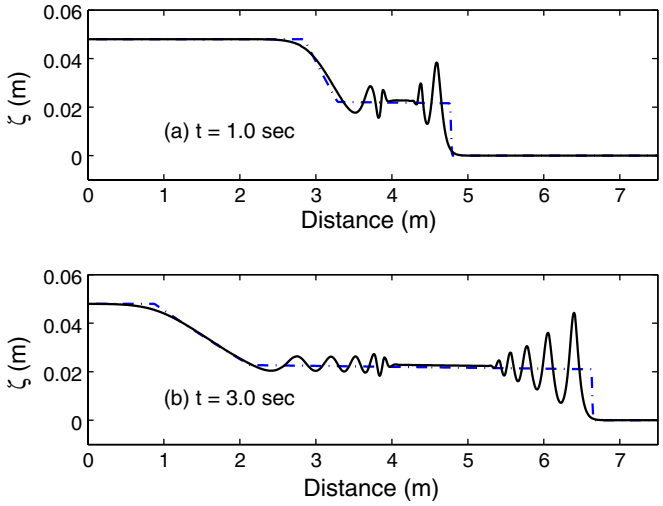

Fig. 6. Computed water surface profiles; solid line: by FNB model; dotted line: by SWE model

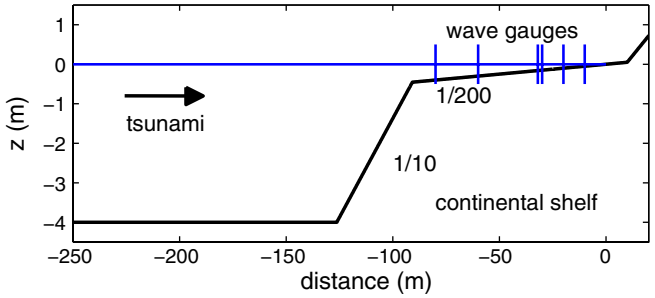

Fig. 7. Experimental setup for tsunami wave fission

depth-integrated model, requiring a modified lateral boundary condition to be integrated into the model, and is not attempted here.

Fig. 6 shows spatial snapshots from both the FNB and SWE simulations. The arrival times predicted by the FNB model and by the SWE model show very good agreement with the measured data. Although the arrival time computed by SWE is closer to the measurement, these results should not be used to conclude that SWE is better than FNB for the prediction of arrival time of surge fronts. As previously mentioned, the reason is that there is nonnegligible difference of t_{op} between the experiment and numerical simulations. In turn, some a difference should be reflected on the results of the arrival times. The computed water-surface elevations by FNB and SWE show nonnegligible differences around the fronts. The height of the leading undular bore wave is 2 times that of the SWE bore result. One more different pattern is detected around the end of the rarefaction wave. As explained with Eq. (1), the unsteady and nonuniform curvature shown in Fig. 6 can cause nonhydrostatic pressure effects. However, these rarefaction dispersion effects are minor compared with those near the front.

J. Hydraul. Eng. 2011.137:754-765.

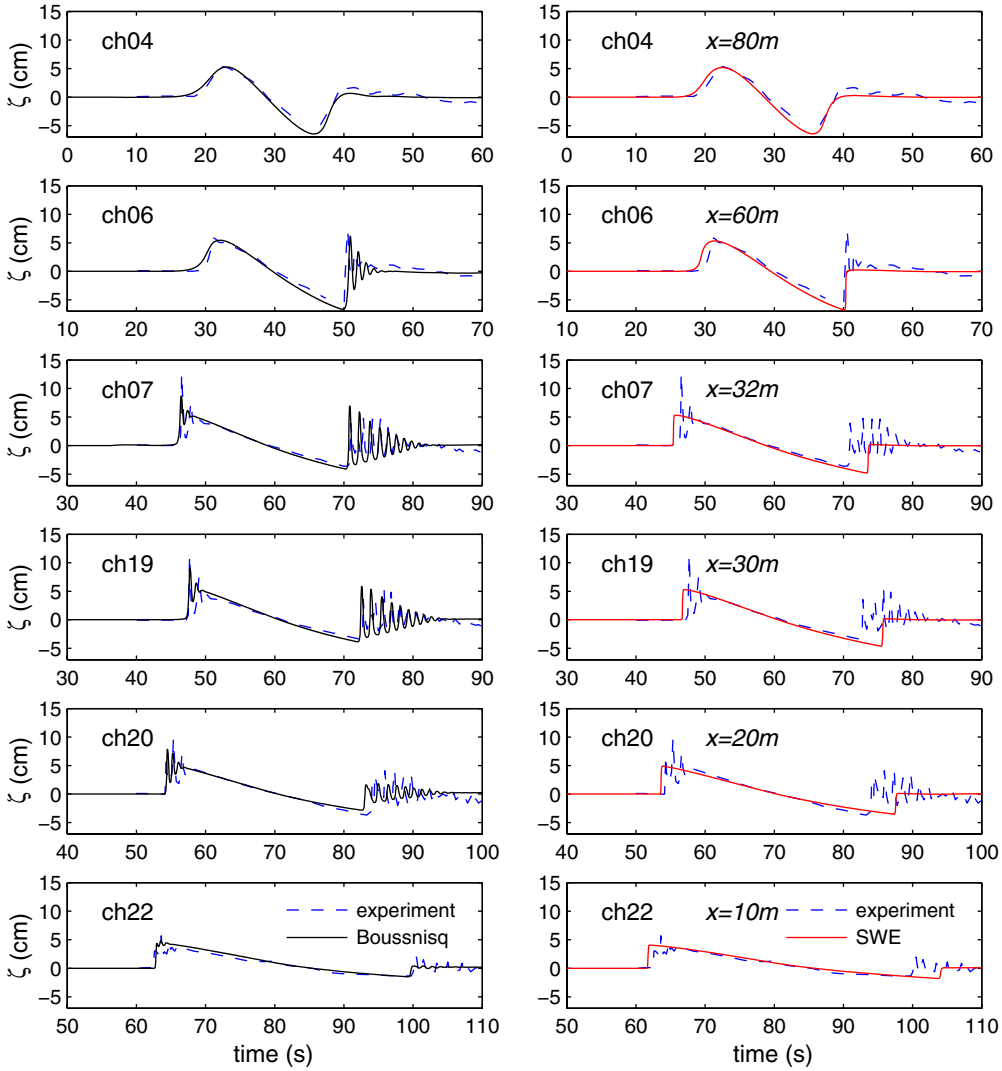

Fig. 8. Time series of water surface elevations (Matsuyama et al. 2007, reprinted with permission from Springer Science+Business Media)

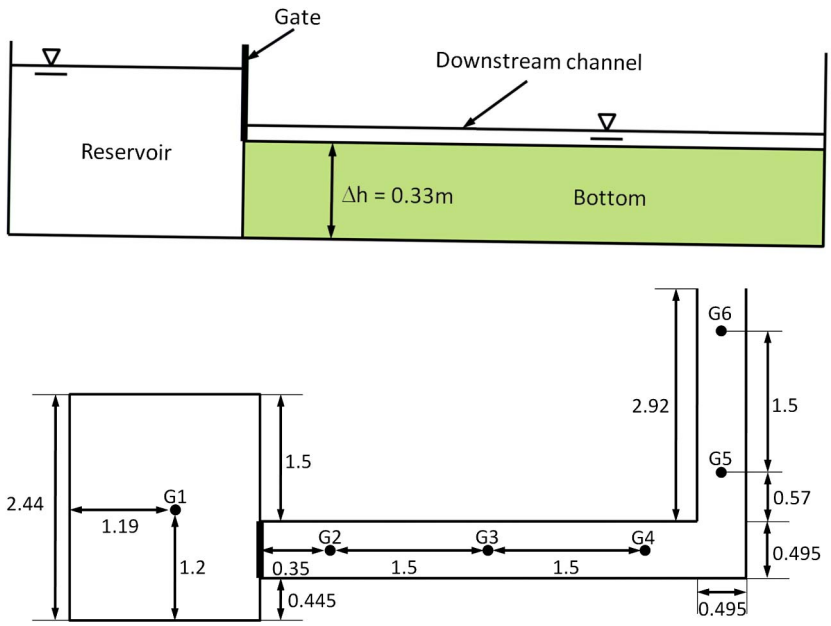

Fig. 9. Experimental setup of the *L*-shaped channel, upper: side view, lower: plan view (all units in meters)

J. Hydraul. Eng. 2011.137:754-765.

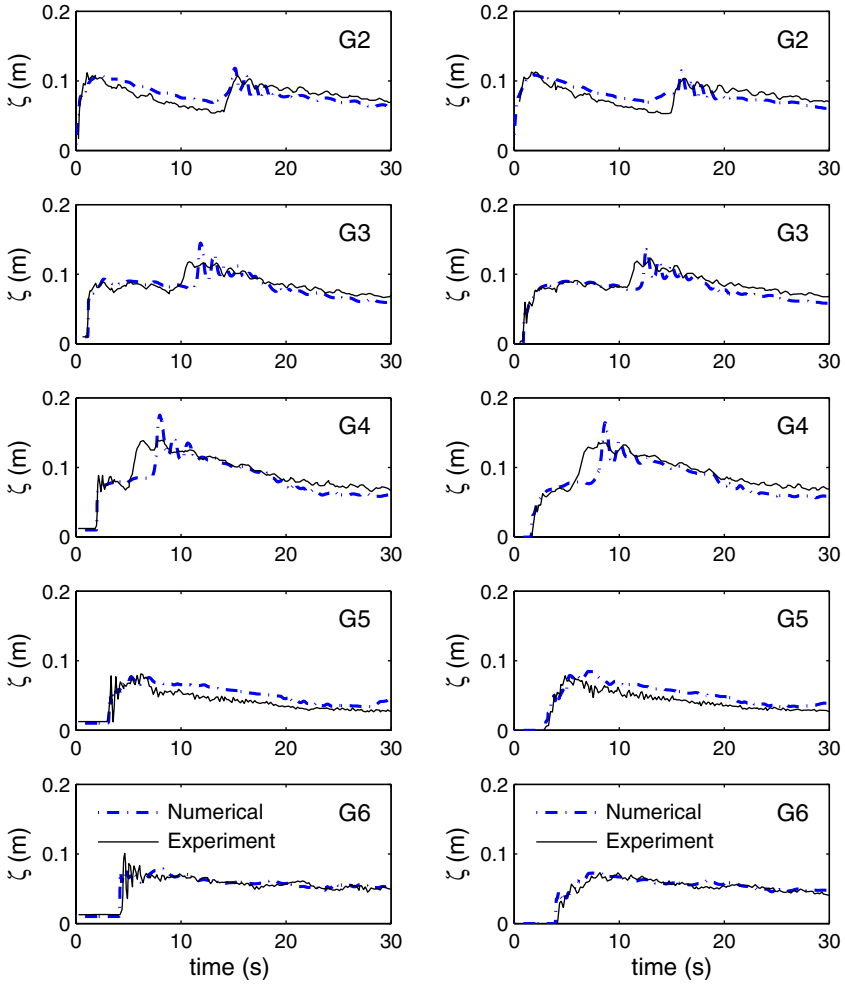

Fig. 10. Time series of water surface elevations in the *L*-shaped channel; left: wet bed case; right: dry bed case; solid line: numerical results, dotted line: measured data

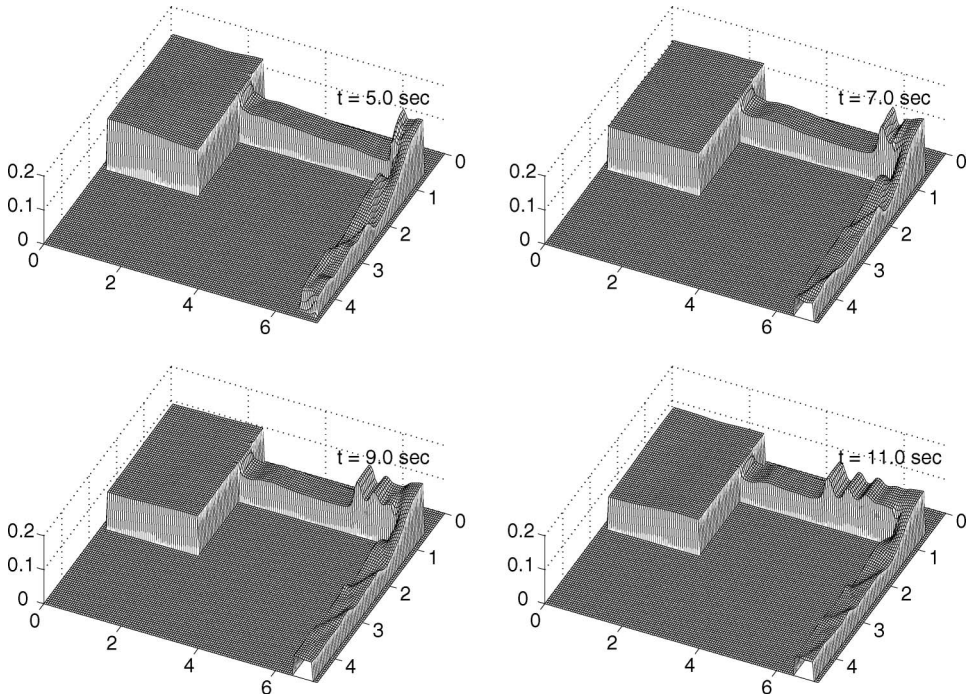

Fig. 11. Snapshots of the computed water surfaces of dam-break flows (wet bed case) (all units in meters)

J. Hydraul. Eng. 2011.137:754-765.

Undular Bores Generated by Tsunami Wave Fission

With the model demonstrated to provide an accurate picture of the physics for the relatively simple, constant-bathymetry, impulsive discharge problems in the previous two sections, a more complex 1HD setup is approached. Here, the model's ability to capture tsunami fission is tested. The general physical background of this process is given in the following. Long wave fission is most commonly discussed in the literature through a solitary wave propagating over an abrupt change in depth, such as a step (e.g., Madsen and Mei 1969; Goring and Raichlen 1992; Seabra-Santos et al. 1987). In these cases, there is a deep-water segment of the seafloor profile, where a solitary wave initially exists. In this depth, the solitary wave is of permanent form. As the solitary wave passes over the change in depth into shallower water, the leading wave energy will try to rediscover a balance between nonlinearity and dispersion; the solitary wave. Since this new solitary wave will be a different shape and contain a lower level of mass, by conservation there must be some trailing disturbance to account for the deficient. This trailing disturbance will take the form of a rank-ordered train of solitons. However, that discussion of fission in this sense is not particularly relevant to "real" tsunami modeling, in which the offshore wave approaching the shelf break rarely resembles a solitary wave solution (Tadepalli and Synolakis 1996). However, the offshore wave does not need to specifically be a solitary wave for this process to occur.

In numerous eyewitness accounts and videos recorded of the 2004 Indian Ocean tsunami, there is evidence of the tsunami approaching the coastline as a series of short period (on the order of 1 min or less) breaking fronts, or strong bores (e.g., Ioualalen et al. 2007). These short-period waves may be the result of fission processes of a steep tsunami front propagating across a wide shelf of shallow depth. This situation is akin to an undular bore, and is identical to that described in the preceding paragraph; it simply takes place over a much longer distance. Each of the leading waves (the translating undular bore), in the nonlinear and shallow environment, will attempt to reach an equilibrium state by which frequency dispersion and nonlinearity are balanced. Thus, the fission waves will appear as solitary waves, or more generally, cnoidal waves. With the large offshore tsunami wave heights possible in extreme events, coupled with a wide, shallow continental shelf, there exists the possibility that this undular bore-fission process may play a much more pronounced role in tsunamis than in flood routing and dam-break situations.

An undistorted experimental study on tsunami soliton fission was carried out in the Large Wave Flume located at Central Research Institute of Electric Power Industry in Japan (Matsuyama et al. 2007). The dimensions of the channel were 205 m long, 3.4 m wide and 6.0 m deep. The bottom geometry and the wave gauges of the experiment are depicted in Fig. 7.

For the numerical simulation, $\Delta x = 0.075$ m, $k_s = 0.0003$ m and $C_r = 0.5$ were used. Additionally, for the consideration of breaking waves, the dissipation model proposed by Kennedy et al. (2000) was employed. The tsunami was generated with a sinusoidal wave form at the left boundary following:

$$\zeta = \begin{cases} A\sin\left(2\pi t/T\right), & 0 \le t \le T \\ 0, & T > t \end{cases} \tag{42}$$

where $A = 0.03$ m and $T = 20$ s. This initial condition is unique in that it is an attempt to recreate the proper length scales of the tsunami studied. Again, this experiment is undistorted. As mentioned previously in this section, most experimental studies use a solitary wave as a tsunami proxy; the aspect ratio of a solitary wave is different by approximately two orders of magnitude as compared to a tsunami in the nearshore. This experiment provides both excellent insight into the nearshore transformation of a nonlinear long wave as well as a benchmark to test numerical codes.

As the long wave is approaching the shore, the transformation processes—the soliton fission—is captured reasonably by the FNB model, as shown in Fig. 8, where the origin ($x = 0$) of the distance is the initial shoreline. Reasonable agreement with the measured data were obtained. The error appears to result mainly the discrepancy of the wave source between the numerical simulation and the laboratory experiment; there is an initial disagreement between the numerical simulation and the data, and this error propagates through the comparisons. As the initial condition, given by Eq. (28), was clearly given by the researchers, no attempt is made to tune this condition to achieve better numerical-experimental comparisons. However, it can be clearly seen that (1) the process of fission at the fronts of the waves is extremely relevant, transforming the wave shape drastically; and (2) the FNB model does a very good job at capturing the general behavior of this process, including wave heights, periods, and number of waves created.

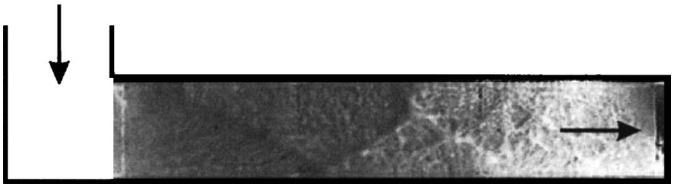

Fig. 12. Secondary shock captured in the experiment (Soares-Frazao and Zech, 2002a, ASCE)

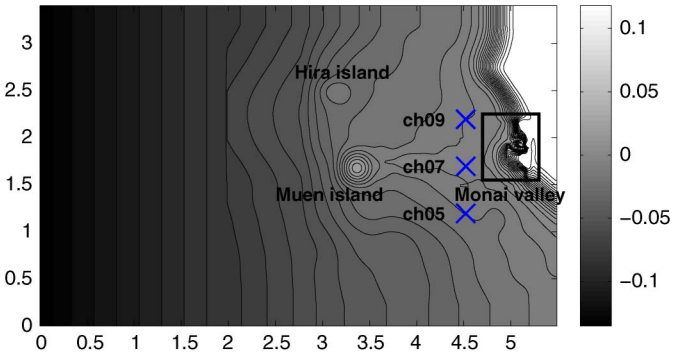

Fig. 13. Plan view contour plot shows the topography data (Matsuyama and Tanaka 2001) (all units in meters)

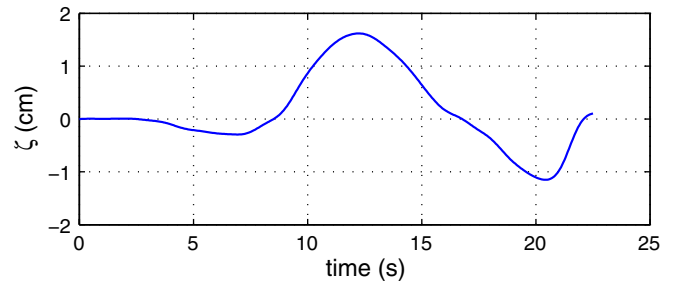

Fig. 14. Time series of the incident wave, located at the left boundary

Dam-Break Flows in an L-Shaped Channel

With model tests for a range of 1HD conditions, including irregular bathymetry and complex incident wave conditions, validation will proceed to 2HD problems. The dam-break flow experiments in an *L*-shaped channel conducted by Soares-Frazao and Zech (1998, 2002a) have been used as a typical benchmark data set for 2HD dam-break flow studies in many publications. The experimental channel shown in Fig. 9 was made up of a 2.44×2.37 m upstream reservoir and a downstream channel with a 90° bend. The bottom of the reservoir and the channel were flat, but the bottom level of the downstream channel was 0.33 m higher than the reservoir bottom. The initial water surface elevation of the reservoir was 0.2 m higher than the channel bottom. For the wet bed case, the total water depth at the downstream channel was 0.01 m. For the dry bed case, it was, naturally, 0.0 m. For the numerical simulation, the $\Delta x = \Delta y = 0.0495$ m and a uniform value of Manning coefficient $n = 0.011$ were used for the entire computational domain, as proposed by Soares-Frazao and Zech (2002a).

The time series of water surface elevation at the gauges are plotted in Fig. 10. Reasonable agreement was obtained, as shown in the figures, although there are small differences between the measured data and the computed results. There are various reasons that can cause the errors. First, Manning's friction factor was used in the numerical simulations, which may introduce some error when the flow is unsteady. As noted by Soares-Frazao and Zech (1998), the computed results were sensitive to the Manning n value. The use of the frictionless side wall condition might contribute to the discrepancy as well. With these deficiencies in mind, the agreement is quite good.

The secondary peaks at the gauges G2, G3, and G4 in the time series can be explained through Fig. 11: the suddenly released

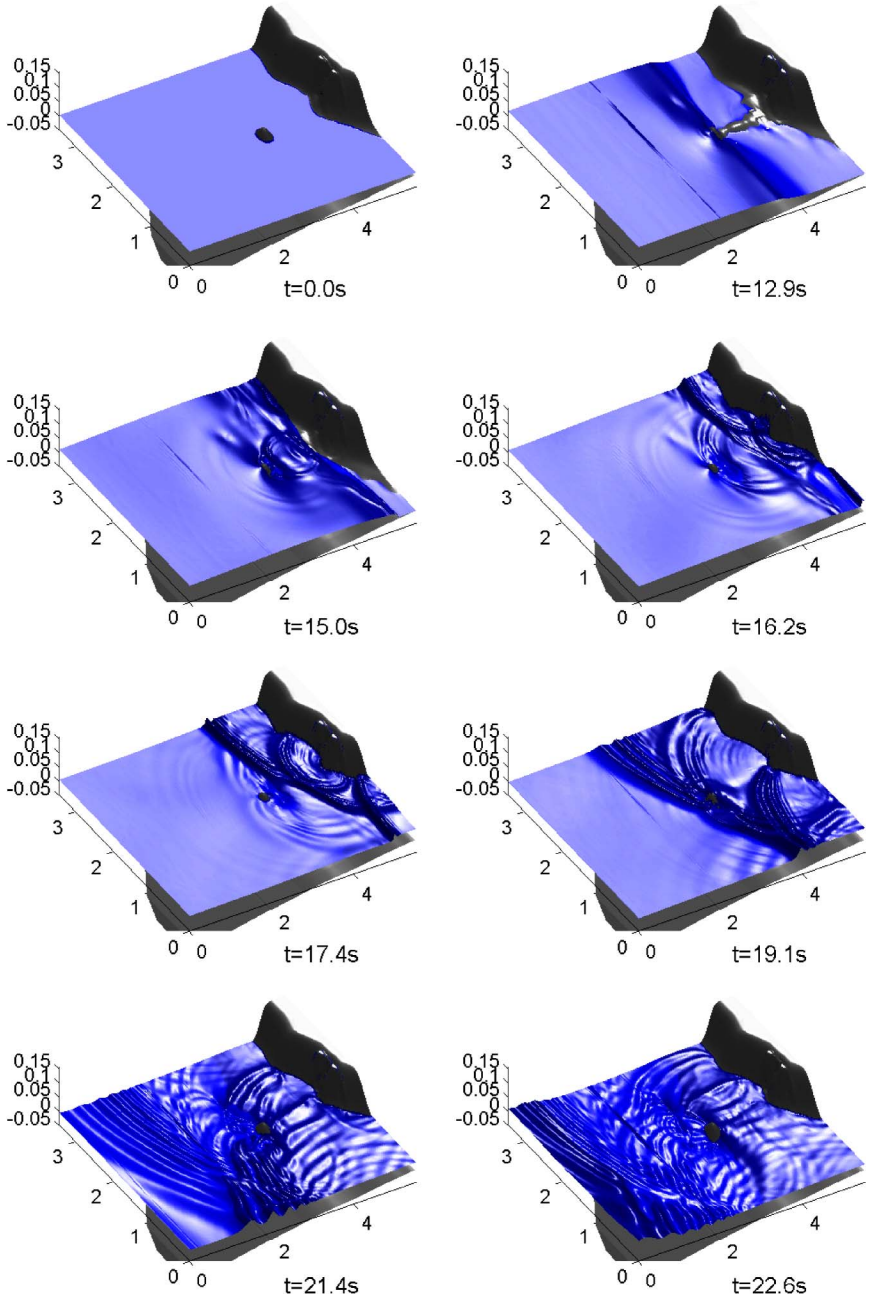

Fig. 15. 3D view of the computed water surface elevations by FNB model (all units in meters)

J. Hydraul. Eng. 2011.137:754-765.

water flows unidirectionally at the beginning and then is blocked by the wall in the bend. The water is temporary stored, and the water surface is increased in the bend. Soon after, the stored water in the bend reverses and propagates to the upstream reservoir, indicating that locally, the flow is subcritical.

After the leading front passes the 90° bend, 2D secondary shocks generated by the reflections between the side walls were captured as shown in Fig. 11. These patterns are similar to the 2D secondary shock captured in the experiments, given here as Fig. 12. Thus, the model developed here is able to predict the nonhydrostatic dynamics that occur at a bore front, as well as 2HD effects.

Okushiri Tsunami Simulation

For a final model test, nonlinear long wave evolution across 2HD-variable bathymetry is examined. On July 12, 1993, a tsunami was generated and struck the southwest coast of Hokkaido, including Okushiri Island. Matsuyama and Tanaka (2001) reproduced the tsunami in a laboratory for the understanding of the maximum run-up height mechanism. This experimental data set is a challenging benchmark problem in the view of both theory and application, as both the wave condition and the topography are irregular and complex. Thus, the data (time series of water surface, animation of run-up process, boundary conditions and bathymetry) were widely spread and used as a benchmark problem (Liu et al. 2008).

The topography given by the laboratory data is plotted in the top plot of Fig. 13. In the domain, there are both a submerged island (Hira Island) and a surface-piercing island (Muen Island). A locally complex topography comprised of two small valleys (Monai Valley) is located on the shore, where the maximum run-up was observed. As shown in the figure, the shoreline is not uniform and so the run-up and the run-down processes should be affected by the particular topography. More details about the experiment are in Matsuyama and Tanaka (2001).

For the numerical simulations, the topography data were used without any modifications or smoothing, and the breaking dissipation was considered. The boundary condition given by the experimental data shown in Fig. 14 was generated by using an internal source wavemaker coupled with an offshore sponge layer at left boundary. At the other boundaries, perfectly reflecting vertical walls were in place. The grid size $\Delta x = \Delta y = 0.014$ m, $k_s = 0.001$ m, and $C_r = 0.5$ were used.

The computed water-surface elevations for the FNB simulations are shown in Fig. 15. At the beginning, withdrawal seaward direction is observed because the wave has a leading depression, or trough. Thus, the water surface elevation decreases and Muen Island is bridged to the shoreline as shown at $t = 12.9$ s. Next, the positive wave from the offshore boundary is propagating toward the shoreline, with Muen Island creating longshore interference. At this time, the dried pathway between Muen Island and the shoreline becomes submerged again. After the wave reaches the shoreline, it is reflected and scattered. As shown at $t = 16.2$ s, the secondary wave that can be captured by dispersive wave model, is propagated into the entire domain. However, from the reflection, the SWE model begins to generate very different secondary wave patterns in the entire domain, as shown in Fig. 16. The SWE model can show only the nondispersive property. Considering the scale of the laboratory experiment is 1:400 (Matsuyama and Tanaka 2001), then the maximum difference of the water surfaces in the domain is approximately 5 m, which number can cause significant engineering problems. In Fig. 15, the wiggle that is parallel to the longshore axis is generated by the submerged vertical cliff located 2 m off the left boundary.

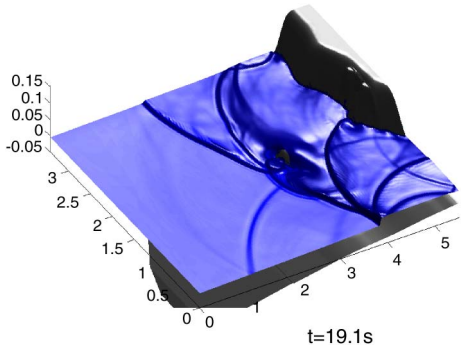

Fig. 16. 3D view of the computed water surface elevations by SWE model (all units in meters)

Finally, and not as a formality, the experimentally measured time series are compared with the FNB results in Fig. 17, where the secondary wave can be seen clearly. As shown in the figures, the numerical results and the measured data are within good agreement including the dispersive wave patterns. The discrepancy was mainly caused by the nonzero initial conditions in the laboratory tank. Delis et al. (2008) and Murillo et al. (2009) also solved

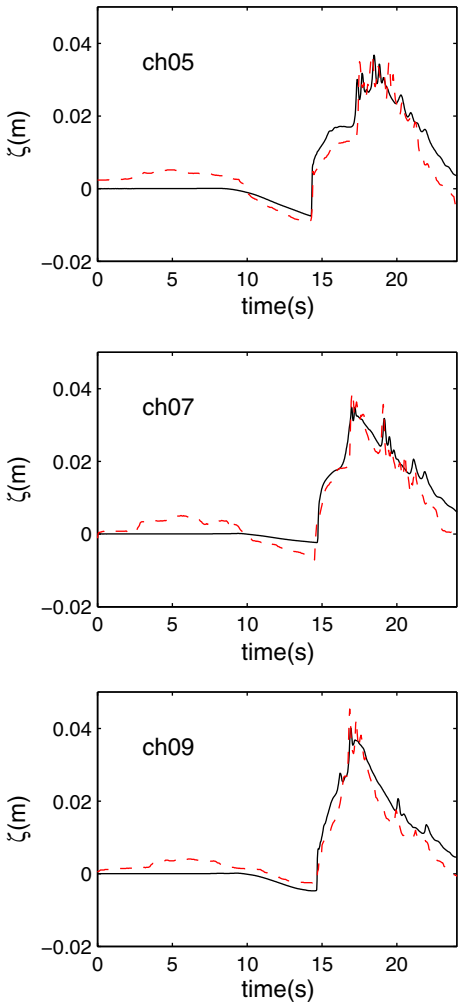

Fig. 17. Time series of water surface levels; solid line: numerical results, dotted: experimental data (Matsuyama and Tanaka 2001); upper: at gauge No. 5 (4.521 m, 1.196 m); middle: at gauge No. 7 (4.521 m, 1.696 m); bottom: at gauge No. 9 (4.521 m, 2.196 m)

J. Hydraul. Eng. 2011.137:754-765.

the same benchmark problem with SWE models and reported reasonable agreements, but no dispersive properties were observed in the results.

Summary

As mentioned in previous sections, the undular motions can lead to significant engineering problems, as the process can increase leading wave crest and flow velocity. To challenge these, a FNB model based on a fourth-order FVM employing the HLL approximate Riemann solver was tested and applied to various typical benchmark problems, including the dispersive and nonhydrostatic effects, in this paper.

In an overall sense, physically reasonable, accurate, and stable computational results were obtained when the FNB that can consider the dispersive and nonhydrostatic pressure effects was used. Some nonnegligible differences were observed from the computed results by the SWE model that are based on hydrostatic pressure assumption. Naturally, the differences can lead to important engineering and design problems. Consequently, the importance of the nonhydrostatic pressure and dispersive effects should be recognized and checked for important hydraulic engineering projects.

Acknowledgments

The research presented here was partially supported by grants from the National Science Foundation (CBET-0427014, CMMI-0619083) to Texas A&M University.

References

Carmo, J. S., Santos, F. J., and Almeida, A. B. (1993). "Numerical solution of the generalized Serre equations with the MacCormack finite difference scheme." *Int. J. Numer. Methods Fluids*, 16(8), 725–738.

Chen, D., and Jirka, G. H. (1995). "Experimental study of plane turbulent wakes in a shallow water layer." *Fluid Dyn. Res.*, 16(1), 11–41.

Delis, A. I., Kazolea, M., and Kampanis, N. A. (2008). "A robust high-resolution finite volume scheme for the simulation of long waves over complex domains." *Int. J. Numer. Methods Fluids*, 56(4), 419–452.

Elder, J. W. (1959). "The dispersion of marked fluid in turbulent shear flow." *J. Fluid Mech.*, 5(4), 544–560.

Goring, D. G. (1978). "Tsunamis—The propagation of long waves onto a shelf." Ph.D. dissertation, California Institute of Technology, Pasadena, CA.

Goring, D. G., and Raichlen, F. (1992). "Propagation of long waves onto shelf." *J. Waterw. Port Coastal Ocean Eng.*, 118(1), 43–61.

Grue, J., Pelinovsky, E. N., Fructus, D., Talipova, T., and Kharif, C. (2008). "Formation of undular bores and solitary waves in the Strait of Malacca caused by the 26 December 2004 Indian Ocean tsunami," *J. Geophys. Res. C: Oceans*, 113(C5), C05008.

Haaland, S. E. (1983). "Simple and explicit formulars for the friction factor in turbulent pipe flow." *J. Fluids Eng.*, 105(1), 89–90.

Ioualalen, M., Asavanant, J., Kaewbanjak, N., Grilli, S. T., Kirby, J. T., and Watts, P. (2007). "Modeling the 26 December 2004 Indian Ocean tsunami: Case study of impact in Thailand." *J. Geophys. Res. C: Oceans*, 112, C07024.

Kennedy, A. B., Chen, Q., Kirby, J. T., and Dalrymple, R. A. (2000). "Boussinesq modeling of wave transformation, breaking, and runup. I:1D." *J. Waterw. Port Coastal Ocean Eng.*, 126(1), 39–47.

Kim, D. H., Cho, Y. S., and Kim, H. J. (2008). "Well balanced scheme between flux and source terms for computation of shallow-water equations over irregular bathymetry." *J. Eng. Mech.*, 134(4), 277–290.

Kim, D. H., Lynett, P. J., and Socolofsky, S. (2009). "A depth-integrated model for weakly dispersive, turbulent, and rotational fluid flows." *Ocean Modelling*, 27(3–4), 198–214.

Lauber, G., and Hager, W. H. (1998). "Experiments to dambreak wave: Sloping channel." *J. Hydraul. Res.*, 36(5), 761–773.

Liu, P. F. (1994). *Advances in Coastal and Ocean Engineering*, 1, World Scientific.

Liu, P. F., Yeh, H., and Synolakis, C. (2008). "Advances in Coastal and Ocean Engineering." 10, *Advanced numerical models for simulating tsunami waves and runup*, World Scientific.

Lynett, P., Melby, J. A., and Kim, D. H. (2010). "An application of Boussinesq modeling to hurricane wave overtopping and inundation." *Ocean Eng.*, 37(1), 135–153.

Lynett, P., Wu, T.-R., and Liu, P. L.-F. (2002). "Modeling wave runup with depth-integrated equations." *Coastal Eng.*, 46(2), 89–107.

Madsen, O. S., and Mei, C. C. (1969). "The transformation of a solitary wave over an uneven bottom." *J. Fluid Mech.*, 39(4), 781–791.

Matsuyama, M., Ikeno, M., Sakakiyama, T., and Takeda, T. (2007). "A study of tsunami wave fission in an undistorted experiment." *Pure Appl. Geophys.*, 164(2–3), 617–631.

Matsuyama, M., and Tanaka, H. (2001). "An experimental study of the highest runup height in the 1993 Hokkaido Nansei-oki earthquake tsunami, U. S.." *National Tsunami Hazard Mitigation Program Review and International Tsunami Symp. (ITS)*, Seattle, 7, 879–889.

Mignot, E., and Cienfuegos, R. (2009). "On the application of a Boussinesq model to river flows including shocks." *Coastal Eng.*, 56(1), 23–31.

Mohapatra, P. K., and Chaudhry, M. H. (2004). "Numerical solution of Boussinesq equations to simulate dam-break flows." *J. Hydraul. Eng.*, 130(2), 156–159.

Murillo, J., Garcia-Navarro, P., and Burguete, J. (2009). "Time step restrictions for well-balanced shallow water solutions in non-zero velocity steady states." *Int. J. Numer. Methods Fluids*, 60(12), 1351–1377.

Nwogu, O. (1993). "Alternative form of Boussinesq equations for nearshore wave propagation." *J. Waterw. Port Coastal Ocean Eng.*, 119(6), 618–638.

Peregrine, D. H. (1967). "Long waves on a beach." *J. Fluid Mech.*, 27(04), 815–827.

Ryu, S., Kim, M. H., and Lynett, P. (2003). "Fully nonlinear wave-current interactions and kinematics by a BEM-based numerical wave tank." *Comput. Mech.*, 32(4–6), 336–346.

Seabra-Santos, F. J., Renouard, D. P., and Temperville, A. M. (1987). "Numerical and experimental study of the transformation of a solitary wave over a shelf or isolated obstacle." *J. Fluid Mech.*, 176(1), 117–134.

Shuto, N. (1985). "The Nihonkai-Chuubu Earthquake tsunami on the north Akita coast." *Coastal Eng. Jpn.*, 28, 255–264.

Smagorinsky, J. (1963). "General circulation experiments with primitive equations, I. The basic experiment." *Mon. Weather Rev.*, 91(3), 99–164.

Soares-Frazao, S., and Guinot, V. (2008). "A second-order semi-implicit hybrid scheme for one-dimensional Boussinesq-type waves in rectangular channels." *Int. J. Numer. Methods Fluids*, 58(3), 237–261.

Soares-Frazao, Sillen, X., and Zech, Y. (1998). "Dam-break flow through sharp bends physical model and 2D Boltzmann model validation." *Proc., CADAM meeting*, HR Wallingford, Wallingford, UK.

Soares-Frazao, S., and Zech, Y. (2002a). "Dam break in channels with 90° bend." *J. Hydraul. Eng.*, 128(11), 956–968.

Soares-Frazao, S., and Zech, Y. (2002b). "Undular bores and secondary waves experiments and hybrid finite-volume modelling." *J. Hydraul. Res.*, 40(1), 33–43.

Toro, E. F. (2002). *Shock-capturing methods for free-surface shallow flows*, Wiley, Chichester, UK.

Tadepalli, S., and Synolakis, C. E. (1996). "Model for the leading waves of tsunamis." *Phys. Rev. Lett.*, 77(10), 2141–2145.

Treske, A. (1994). "Undular bores (Favre-waves) in open channels—experimental studies." *J. Hydraul. Res.*, 32(3), 355–370.

Vischer, D. L., and Hager, W. H. (1998). *Dam hydraulics*, Wiley, Chichester, UK.

Wei, G., Kirby, J. T., Grill, S. T., and Subramanya, R. (2006). "A fully nonlinear Boussinesq model for surface waves. Part 1. Highly nonlinear unsteady waves." *J. Fluid Mech.*, 294(-1), 71–92.

Yamamoto, S., and Daiguji, H. (1993). "Higher-order-accurate upwind schemes for solving the compressible Euler and Navier-Stokes equations." *Comput. Fluids*, 22(2–3), 259–270.

J. Hydraul. Eng. 2011.137:754-765.